Optimizing data usage in regional body wave tomography by using asynchronous network data and relative sensitivity kernels: an example from Patagonia

Walid Ben-Mansour[(1)],Valerie Maupin[(2)]

[1]Washington University in Saint Louis, Department of Earth, Environmental and Planetary Sciences, MO, US,

[2]PHAB – Centre for Planetary Habitability, Oslo, Norway

Corresponding author: walid@wustl.edu

Optimizing data usage in regional body wave tomography by using asynchronous network data and relative sensitivity kernels: an example from Patagonia

Walid Ben-Mansour[(1),] Valerie Maupin[(2)]

1. Washington University in Saint Louis, Department of Earth, Environmental and Planetary Sciences, MO, US,
2. PHAB – Centre for Planetary Habitability, Oslo, Norway

Abstract:

A very frequent approach for studying lithospheric processes is to deploy temporary seismological networks in dedicated areas and to map the mantle structures with different approaches. One of them is the well-established relative travel time body wave tomography. Different circumstances often lead to a non-uniform deployment of stations both in space and time, and a wish to combine data which have been acquired asynchronously. This is the situation in Patagonia where two distinct seismic experiments provide complementary seismic data over the region covering the Patagonia slab window. Combining these data in one regional relative body wave tomography is however problematic as the two data sets are a priori with respect to two different reference models. In this contribution, we show that the number of finite-frequency relative travel time residuals varies very strongly from station to station for this data set, violating the assumption implicit in relative travel time tomography of a unique reference model due to an even data distribution for all events. We demonstrate the superiority of the inversion using relative sensitivity kernels compared with a traditional approach with absolute kernels and event terms. A resolution test proves how this is crucial for resolving the important issue of the eastern extent of the slab window. In addition, we discuss potential issues related to interference of the direct phases with core phases when measuring finite-frequency travel time residuals by cross-correlation of waveforms in necessarily relatively large time windows. We also briefly outline our preferred strategy for performing crustal correction, keeping in mind that finite-frequency residuals require frequency-dependent crustal corrections.

1. Introduction

Body wave tomography has given us a detailed picture of the 3-D structure of the mantle both at global scale and at regional scale in different geodynamics settings. The increase in resolution in recent models is due partly to novel methodologies which allow to exploit more phases with for example full waveform inversion [Tromp et al. 2005; Fichtner et al., 2013; Tromp 2020], but also very importantly to the increase in data availability through major data collection efforts such as USArray [IRIS Transportable Array 2003] or SinoProbe [Dong et al. 2013] and curation of existing ones [Engdahl et al. 2020]. Although the resolution of global models is increasing, regional models are still often superior in terms of resolution, justifying the common installation of regional temporary networks for dedicated study of specific tectonic/geodynamical targets such as the Alpine region with the AlpArray experiment [Hetenyi et al., 2018], Fennocandia with ScanArray [Thybo et al., 2020], or the Pyrenees with both PYROPE experiment [Chevrot et al., 2017] and IberArray [Diaz et al. 2009]. These data are commonly exploited using standard seismological techniques like surface-wave tomography, SKS-splitting analysis, receiver-function analysis, and body-wave tomography. In the present paper, we would like to highlight how we have overcome some of the challenges commonly encountered with data selection and processing in regional body-wave tomography.

Regional body-wave tomography was introduced by Aki et al. (1977) and is still often referred as ACH-tomography. Its main principle is to build a 3-D local model beneath a seismological network by inversion of relative traveltimes between the stations, assuming errors in source times locations and large-scale heterogeneities affect all travel times similarly and therefore cancel out when measuring relative times. As very thoroughly detailed in Aki et al. (1977) and commonly acknowledged, this results in models with unknown vertical average and where only relative variations at a given depth should be interpreted. Another related point is that the model is with respect to the average model beneath the network. As long as all events are recorded at almost all stations, this is not an issue. When some stations are out-of-function for a longer period of time, or record only a few events, it might become unclear if these stations should be included in the data set or not, as the average model seen by the data will differ from event to event. An extreme case is when different networks, covering different parts of the study region, have been functioning at different times and therefore record different events. This is quite a common situation, when data from different experiments done successively would benefit from being combined.

This is the situation in Patagonia, at the southern end of the South American continent, where two temporary seismological networks were deployed, first in 2005-2006 over a region of about 400 km by 200km size close to the present-day location of the Chilean triple junction (**Figure 1**) and in 2018-2021 to study the Patagonia slab window and the mantle properties beneath the Patagonia icefield in addition of new broadband seismic stations as part of the new permanent Chilean seismic network since 2015.

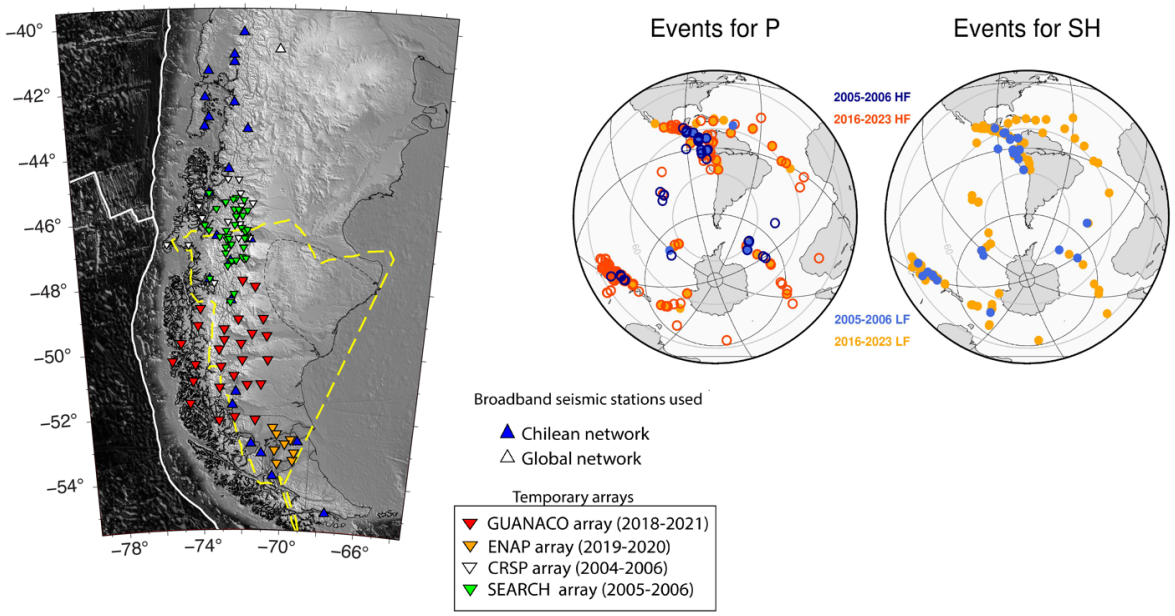

Figure 1. *Topographic map of Southern Patagonia with broadband seismic stations used in this study. Teleseismic events used in the finite frequency body wave tomography. The events recorded by the early network (2006-2006) are shown in blue, with a full circle when used in the low-frequency range and with a darker blue open circle in the high-frequency range. The same in orange for the events recorded by the more recent network (2016-2023).*

Data from the earlier networks have been used in a regional scale P wave travel time tomography by Russo et al (2010) and Miller et al. (2023) showing the presence of low velocity anomaly between 46°S and 47°S associated with the slab window and fast velocity anomaly north to the Chilean triple junction associated with the Nazca slab. Russo et al (2010) also analyze shear wave splitting to interpret the upper mantle flow pattern associated with the slab window with ENE-WSW fast direction in the middle of the slab window and NE-SW trends south of the slab window. Recently, surface waves analysis [Mark et al., 2022] using the later network provided a better constraint on the southern extension of the slab window and a new regional scale crustal model including both crustal thickness and new information on the thickness of the Australe-Magallanes basins. Using later network and re-processing older networks for shear wave splitting analysis, Ben-Mansour et al. (2022) show a strong E-W fast

direction south of the Chilean triple junction and the edge of the subducting Nazca slab. Most of south Patagonia show NE-SW fast directions consistent with large-scale asthenospheric flow. A recent P-wave tomography by Kondo et al. (2024) combines these data with ISC data and data from permanent stations to derive a model at combined global and regional scale. Ben-Mansour et al. (2025) present the results of a P and SH regional body-wave tomography done using a combination of data from the two sets of networks and some permanent stations using relative kernels.

In the present paper, we would like to present the methodological elements that we have developed for tomographic analysis of asynchronous data, which can be of general interest to the community. The core of the methodology to combine data from different networks is to use relative kernels, which account for the data distribution individually for each registered event, as discussed in Maupin and Kolstrup (2015), following the formulation of Aki et al. (1977). The efficacy of the methodology was demonstrated with synthetic data in a very schematic model in Maupin (2021), showing that combining asynchronous temporary arrays in regional scale body wave tomography is not a trivial problem and tomography may yield biased models if not conducted with relative sensitivity kernels. In addition to the original paper of Aki et al. (1977), where relative kernels were applied to data from the NORSAR array, relative kernels were applied recently to real data in Veisi et al. (2021). We confirm here their efficacy to combine asynchronous data by analyzing the results of a real data case and compare with an alternative procedure using absolute kernels and event terms. We first present the data set that we have used and the challenges related to its very uneven data distribution. Although relative kernels can be designed using ray theory, we have worked with finite-frequency kernels. This implies measuring the relative travel times in different frequency bands and allows us in particular to use rather low frequencies also for P waves. We will present some examples of relative kernels and how they allow us to include all the available data. Using finite frequency instead of picking arrival times, interference of neighboring phases might bias the residuals for some epicentral distances and we will discuss how we have addressed this issue. Some short elements concerning the frequency-dependent crustal correction will also be presented.

2. Asynchronous datasets

Our data come from a very heterogeneous data set with twenty-two widely distributed permanent stations, two compact early networks and a later deployment covering a larger

region (**Figure 1**). Combining those has the advantage of getting the bigger picture, still benefiting from the better resolution offered by the more compact networks. Between 2004 and 2006, two broadband seismic arrays (CRSP and SEARCH experiment) covering an area of 400 km by 400 km were deployed north to the Chilean Triple Junction. The CRSP deployment provides the first geophysical imaging of the slab window from body wave tomography and the mantle flow pattern from shear wave splitting analysis [Russo et al., 2010]. The SEARCH experiment did not provide any additional information on the geodynamic setting of this region but extended the seismic model to the east. Between 2018 and early 2021, the deployment of twenty-six broadband instruments south to the triple junction from 44°S to 53°S to bring new datasets in South Patagonia allowed to map the southern extension of the slab window from surface wave tomography and give a new crustal model [Mark et al., 2022]. Meanwhile, new broadband seismic stations were deployed in Chile as part of the new permanent network since 2016 with twenty-two new seismic stations between 40°S and 56°S. Four seismic stations were deployed in Tierra del Fuego by the Empresa Nacional del Petróleo (ENAP) and provide an additional twelve months of data in 2019. We also include the permanent station PLCA, part of the Global network, which provides additional data between 2004 and 2006 and more recently between 2016 and 2023.

3. Selection of events and measurements of residuals

Relative finite-frequency travel time residuals were measured following mostly the procedure described in Kolstrup and Maupin (2015), which combines the Iterative Cross-Correlation and Stack (ICCS) algorithm of Lou et al. (2013) with the Multi-Channel Cross-Correlation method (MCCC) of VanDecar and Crosson (1990). The ICCS algorithm calculates an array stack from predicted arrival times, cross-correlates each seismogram with the array stack to find the time lags at maximum cross-correlation. Each individual trace is aligned according to the time lag and relative to the stack in an iterative procedure where the stack is updated for each iteration. After alignment by ICCS, the cross-correlation coefficient and mean spectral coherence between each trace and the stack are calculated. A weighted average of the two is computed and traces with a value lower than a user-defined cut-off (usually about 0.5) are excluded. This procedure rejects data with a significantly different shape than the array stack. The MCCC algorithm [VanDecar and Crosson, 1990], used in the end on the already well-aligned traces, cross-correlates each possible pair of seismograms and uses a least-squares method to calculate an optimized set of possibly additional residuals. The additional residuals are in

practice almost always negligible, but this final step has the advantage of providing error-bars to each measurement to be used as weights in the tomographic inversion.

We selected events larger than Mw5.4 in the epicentral range 28º and 98º. We band-pass-filter waveforms around the secondary seismic noise peak ~0.2 Hz which dominates the signal. Here we use two frequency bands for P but only one for S. Our experience is that two smaller frequency ranges for S, as in Kolstrup and Maupin (2015), lead to more monochromatic waveforms and a larger risk of cycle-skipping, but no clear benefit in amount of data. This is different from the P wave where we see a clear benefit in using two frequency bands. Regardless of the fact that these two frequency bands have different sensitivities to the structure, and therefore contribute differently to the inversion, they also have a different noise level. Although the noise level is in general lower in the high frequency range, it is not always the case. Some travel times which could be measured only in the low frequency range were very useful for filling some azimuthal gaps, data which would have been rejected with ray theory phase picking.

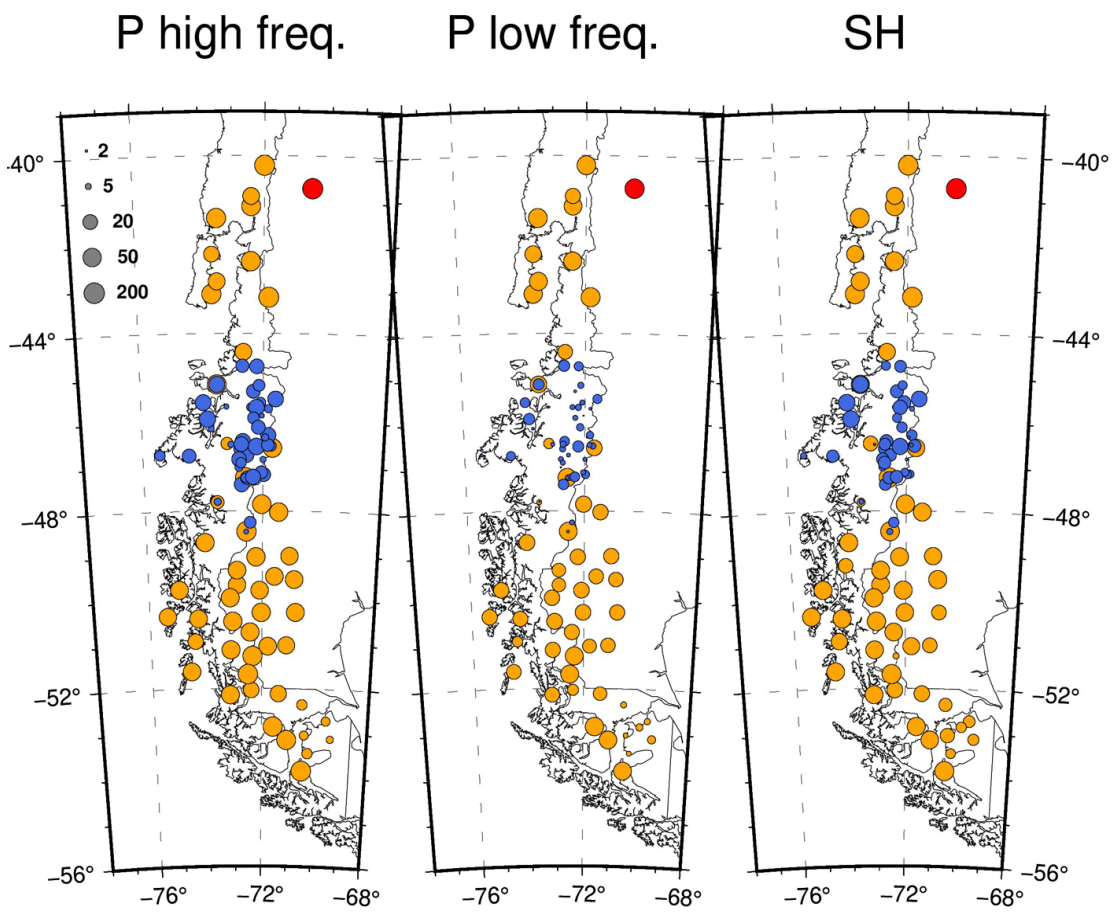

Figure 2. *Number of residuals having passed the selection criteria at the different stations for P waves (high and low frequency ranges), and for SH waves. In order to damp the dominance of the stations with many data, the size of the dots is proportional to atan(N/10) where N is the number of residuals, as illustrated with grey dots on plot a. Blue dots correspond to stations from the early network, orange ones from the late network, and the red dot to permanent station PLCA which recorded during the whole period.*

Figure 2 shows the amount of data available at the different stations in the different frequency bands, varying from 169 data at station PLCA for P waves in the high-frequency band down to 1 in a few cases. Some stations from the 2005-2006 network have a particularly low number of detections, but this is compensated by the fact that they are closely spaced. By using relative kernels, we can use all these data and do not need to discard some stations because they have few data, or fair for a bias in resolution because the station density irregularity.

4. Relative kernels for Finite frequency body wave tomography

To solve the inverse problem from relative travel times to relative seismic velocity anomalies, we follow the data-adaptive, multiscale, finite-frequency tomography described in detail by Hung et al. (2011). This includes the computation of the 3-D Born-Fréchet (absolute) kernels which express the influence of velocity heterogeneities on finite-frequency travel times [Dahlen et al., 2000; Hung et al. 2000; Schmandt and Humphreys, 2010; Maupin and Kolstrup, 2015]. Our procedure has a simple additional step compared to previous studies corresponding to the computation of the relative kernels from the absolute ones. The relative kernels are simply the absolute ones minus the average of the absolute kernels corresponding to data from a given event. This ensures consistency with the data, which are by construction relative demeaned travel times.

We recall here briefly how they are constructed. We denote by K_c the ordinary "banana-doughnut" kernels, where c stands for α in case of P waves and β for S waves. They show the sensitivity of the absolute traveltimes of P or S waves to the structure along their path from one source to one station. The relative kernels K_c' are defined as a function of the absolute kernels K_c as:

$$K_c'(\vec{x}) = K_c(\vec{x}) - \overline{K_c}(\vec{x})$$

where $\overline{K_c}$ is the average of the kernels associated with a given event:

$$\overline{K_c}(\vec{x}) = \frac{1}{N} \sum_{stations} K_c(\vec{x})$$

and N is the number of stations having recorded that event.

They are illustrated with 4 examples in Figure 3. The kernel in Figure 3a is associated with the P-wave residual at high frequency at station ES3R for an event in Guatemala. The event was registered during the second period of station deployment, with stations located in the North and South of the study region with a gap in between. The kernel has large positive values beneath ES3R, showing a strong dependence on the structure beneath this station, but we can also notice negative values spread in the whole region, corresponding to locations of stations that have registered the same event. These negative values express that the residual measured at station ES3R is with respect to the residuals measured at the other stations, and that its value therefore also depends on the structure beneath these stations.

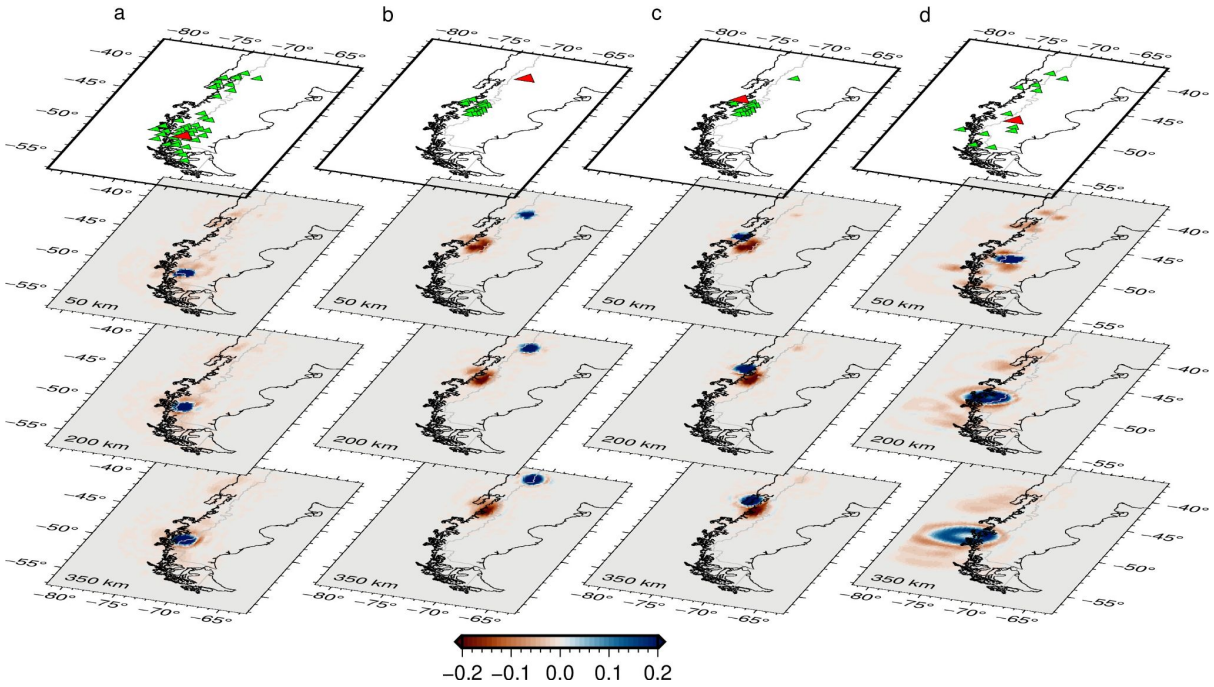

Figure 3. *Relative sensitivity kernels for 3 cases of high-frequency P-wave data (plots a to c) and one case of S-wave data (plot d). The upper panels show in red the station at which the data has been recorded and in green the other stations having recorded the same event. The other panels show the relative kernels at three selected depths with a color scale truncated at 20% of the maximum value of the 3D kernel for better visualization*

Figure 3b shows the kernel for the residual at station PLCA for an event in Ecuador registered during the early period of deployment, when station PLCA was supplemented by a network of stations grouped close to 46°S. The positive kernel values beneath PLCA are associated with a strong patch of negative values where the other stations are grouped. This expresses that the relative residual at PLCA depends on the contrast in structure between this station and

231 the region further South. For the same event, the kernel of the residual at station AGU01,
232 located in the group of stations, is shown in Figure 3c. Although a small negative value is
233 visible beneath PLCA, this kernel dominantly expresses that the residual at AGU01 depends
234 on the contrast in structure between the region to the Northwest of the group of stations, where
235 AGU01 is located, and the rest of the region beneath the network.
236
237 Figure 3d shows an example of kernel for an SH wave recorded at station WIND. For this
238 event on the South Pacific Ridge, 13 residuals were measured at stations rather well
239 distributed in the whole region. This small number of residuals leads to a kernel with clear
240 positive values beneath WIND and rather clearly identified smaller negative values at the other
241 stations having recorded the event.

242 ## 5. Comparison of tomographies with absolute and relative kernels

243 As illustrated in Figure 3, the relative kernels are non-zero in a much larger part of the model
244 than the absolute ones. Inverting with relative kernels requires therefore to deal with a less
245 sparse matrix compared to using absolute kernels, increasing the computational cost. An
246 alternative procedure to combine heterogenous data used for example by Bezeda et al. (2010)
247 and Youssof et al. (2015) is to invert with absolute kernels and consider the average delay per
248 event as an event term. As most software include event terms, this new term can be absorbed
249 in the usual event term, allowing to use standard software without any modification.
250
251 This means that we have two options to account for the average term. We can incorporate it
252 in the kernels by building the relative kernels presented in the previous section and invert only
253 for the model parameters *dc* using the relative kernels to express the sensitivity of the data to
254 the model:
255 $$\delta t = \int K_c'(\vec{x}) dc(\vec{x}) dx$$
256
257 Or we can single out the average term, and, as this term is common to all stations for a given
258 event, consider it as an event-characteristic term. This so-called event term accounts for the
259 average structure beneath the stations which have recorded this event, giving the inversion
260 some flexibility to adjust the model to a different average structure for each station
261 configuration. Although it does not have the traditional meaning of the term (possible errors in
262 event location and timing, and in structure outside the inverted model), it can be incorporated
263 in the traditional event term and does not require any additional element in the inversion. This
264 leads to an inverse problem of the form:

$$\delta t = \int K_c(\vec{x}) dc(\vec{x}) dx + E_t$$

where we invert for the model parameters *dc* using the absolute kernels and for an additional event term E_t. This term is considered as an independent parameter in the inversion although it depends in reality on the structure through:

$$E_t = -\frac{1}{N} \sum_{stations} \int K_c(\vec{x}) dc(\vec{x}) dx$$

This shows that inverting with the event term introduces an artificial trade-off between the parameters of the inversion, a drawback avoided with relative kernels.

Inverting with event terms leads to the correct solution for the small test case given in Maupin (2021) section 2.2 provided the event terms are given a much larger weight in the inversion than the slowness values. We proceed with more realistic resolution tests to compare the performance of relative and absolute kernels inversion. Figure 4 shows the results of four resolution tests for two synthetic models, L1 and L2, varying the weights of the event terms. Figure 5 shows the distribution of the values of the event terms for these inversions for model L2, with an additional case with very little weight on the event term. The event terms for model L1 and for the real data are shown in the appendix. In all cases, the inversion also includes station terms with weight 100. Their values are shown in the appendix.

Let us first precise some technical elements of importance concerning the resolution tests. The residuals are computed by combining the sensitivity kernels, either absolute or relative, with the synthetic model and then demeaned event by event in order to simulate the actual data procedure. The demeaning is also done when using relative kernels, although it is actually unnecessary in this case. We have checked that the residuals computed with absolute kernels and demeaned are strictly identical to those computed with the relative kernels. In addition, noise with a standard variation of 0.04s, derived from data analysis, is added prior to inversion.

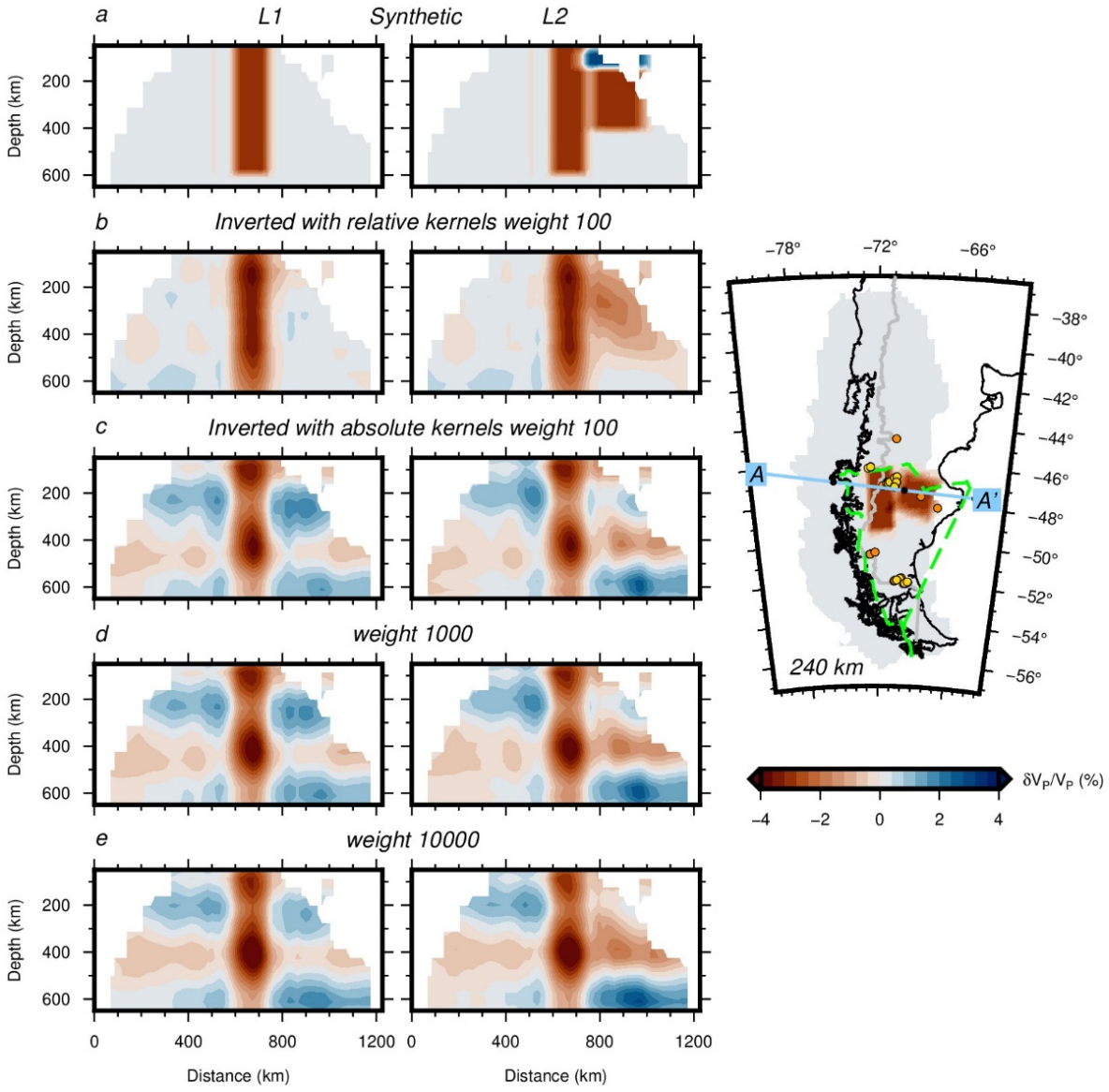

Figure 4. *Resolution tests to compare inversions with relative and absolute sensitivity kernels. The synthetic models L1 and L2 are shown in the two upper plots and L2 in the map to the right-hand side. The map also shows the proposed contour of the Patagonia slab window as a green dashed line and the location of recent magmatism as orange dots. The inverted models are shown in plots b for inversions with relative kernels and event weight 100 and in plots c to e for inversions with absolute kernels and event weights 100 to 10000. The models are only shown in regions with resolution of at least 1% of the maximum of the resolution matrix.*

The inversions with the relative kernels are the only ones that can clearly distinguish between the two tests models. They have far less spurious oscillations with depth than those obtained with the absolute kernels. The average model with depth is not constrained when inverting relative residuals and vertical sections can therefore be biased by a wrong average depth

model with for example oscillations. We interpret the emergence of these depth oscillations as a result of the inversion forcing a zero-mean model at different depths for inversion with absolute kernels, whereas this is not required for inversions with relative kernels, since the kernels are themselves zero-mean, as already discussed in Maupin (2021).

The models resulting from the inversions with absolute kernels are not very different from each other, although the deep low velocity zone to the East in model L2 is slightly better rendered with the largest weight on the event terms. The weight has a very large incidence on the values of the event terms. Using absolute kernels, the event terms are negligible for a weight of 1 (Figure 5 a) and increase to values between -5 and 5 seconds for a weight of 10000 (Figure 5 e).

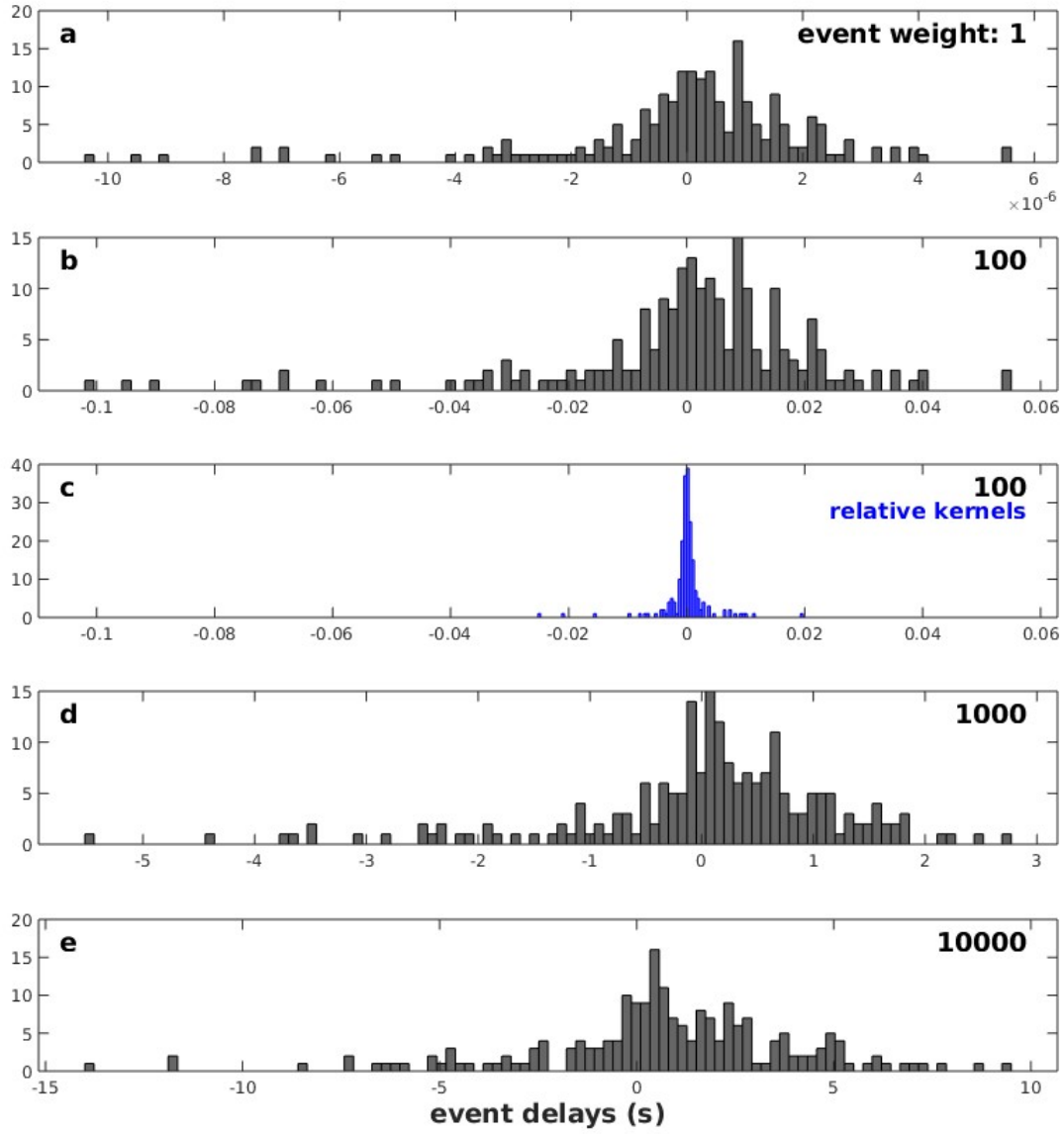

Figure 5. *Plots a, b, d and e: histograms showing the values of the event terms for inversions with absolute kernels and different weights for the event terms for model L2. Note that the horizontal scales are different for the different weights. Plot c in blue: inversion with relative kernels and event term weight 100, at the same horizontal scale as plot b.*

The average residuals per event in model L2 reach large values of up to 0.85 seconds for a few events that happen to be recorded mostly at few stations located above the heterogeneiety, but otherwise vary from 0 to 0.2 seconds for 80% of the events (Figure 6). The events term for a weight of 10000 correspond therefore to an underdamped solution with respect to the event terms. The range of values is more correct for inversions with weights of 200 to 300 (Figure 6), but the inverted terms are often quite different form the real mean residuals and most importantly the velocity models obtained with this damping of the event terms do not vary significantly from models obtained without event terms. It appears therefore that using event terms for absorbing the heterogeneity in the station distribution is not a very good strategy. This might result from the trade-off between velocity and event terms.

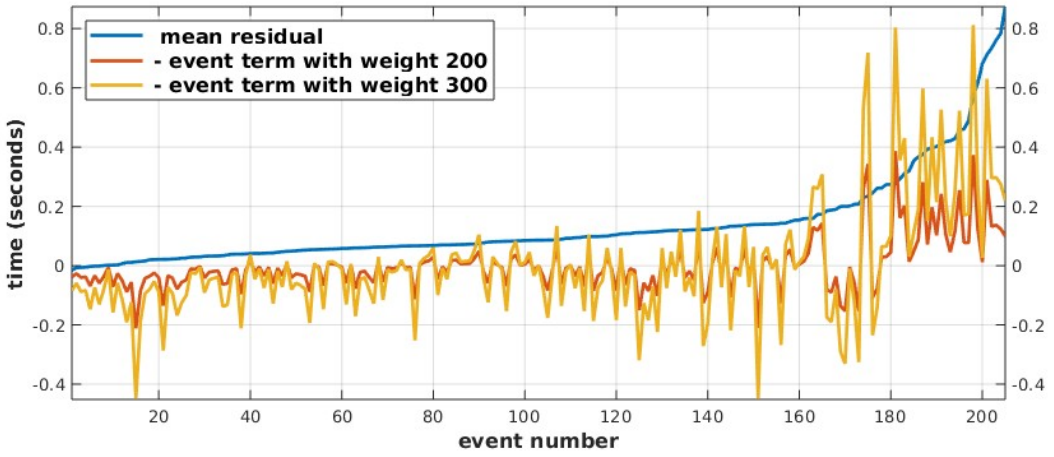

Figure 6. *Comparison of the mean residuals per event for model L2 and minus the event terms after inversion with event terms weights of 200 and 300. The events are sorted per increasing mean residual. A general change in the mean model, which cannot be resolved with relative residuals, will produce a vertical shift of the lines. This can explain why the event terms are in general lower than the mean residuals. We observe in general an increase of the event terms for events with larger mean residuals, but with large variations.*

Using the same weight of 100 for the event terms, the inversion with relative kernels (Figure 5 c) leads to event terms one order of magnitude smaller than inversion with absolute kernels (Figure 5 b). This shows that, even though they do not help much in improving the model, the

event terms play a role in absorbing part of the residuals in the inversion with absolute kernels. Theory says that they are not needed with relative kernels, and this is confirmed by the much smaller values they get in that case after inversion.

In order to study the influence of using relative kernels instead of absolute ones with the real data and to test the resolution gained by adding data from the earlier networks, we have performed two tomographies of the P-wave data in addition to the one done with all the data and the relative kernels, presented in Ben-Mansour et al. (2025). In the first case, we use all the available data, but inverts with absolute kernels instead of relative ones. In the other case, we use only data from the later network, in orange in Figure 2. In all cases we use station and events terms with weights of 100. We refer to Ben-Mansour et al. (2025) for more details on the parameters of the inversion and for a discussion of the model itself and its geodynamical implications. We restrict ourselves here to an analysis of the differences between the three models, shown at 200 km depth in Figure 7.

Although we do not combine data from different networks, we have still performed the inversion of the reduced data set with relative kernels. This ensures that the differences we see are related to the difference in the data set, and not in the methodology. In addition, even without combining data from different networks, not all stations have good data for all events, and every event in practice corresponds to a slightly different set of stations. This alone justifies using relative kernels.

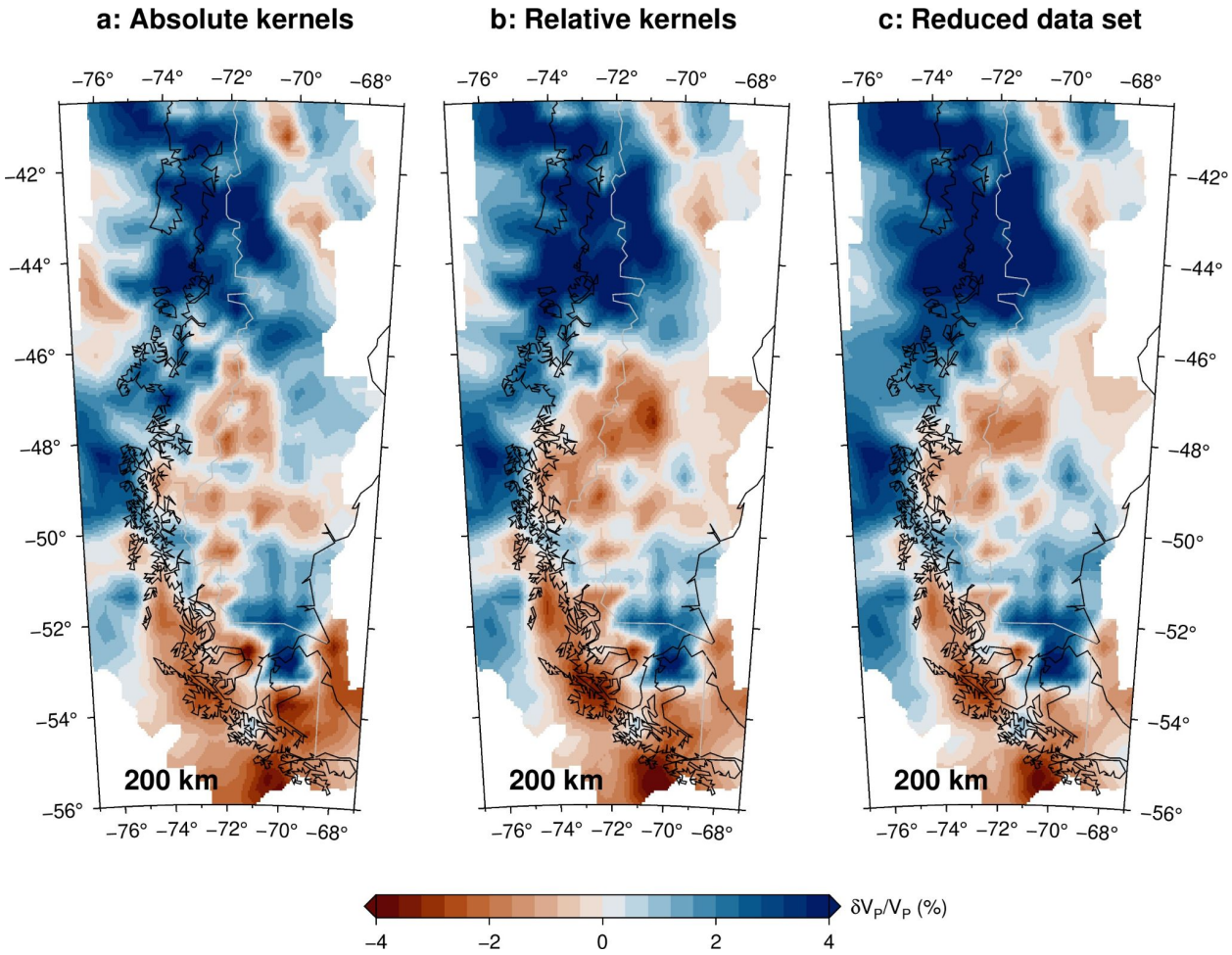

Figure 7. *Maps at 200 km depth of P-wave models resulting from the inversion of the full data set with absolute kernels (plot a), relative kernels (plot b), and (plot c) a data set reduced to late events (2016-2023, see Figure 1).The models are shown only in regions with resolution of at least 1% of the maximum of the resolution matrix.*

The differences between the models are not drastic, but still clearly visible. Keeping only the later data provokes a data gap of about 2° at the southern end of the Nazca slab, in a region which is crucial from a geodynamical point of view. This model (plot c) does not show a significant degradation in the resolution of the area of the gap compared to the one using all data (plot b), possibly because the major geodynamic boundary is by chance in the middle of the gap, a position that would be favored by default by an inversion. The model has slightly stronger high velocities and slightly weaker low velocities, corresponding to a slight change in the average model. As noted earlier, models derived using relative kernels do not need to have zero mean, but the average is not resolved by the data and should anyway not be interpreted.

The model including all data but using the absolute kernels for inversion (plot a), has more subdued large-scale features compared with the model using relative kernels (plot b). This can best be seen in the high-velocity region corresponding to the Nazca slab (42° to 46°S), and in the low-velocity region at (48°S-72°W). This is consistent with the results of the synthetic experiment in Maupin (2021), showing that usage of relative kernels improves the large-scale rendering of the inversion.

Another noticeable difference between plots a and b in Figure 7 is the presence of a negative anomaly at about 69°S-49°E in the inversion with relative kernels whereas it is positive in the inversion with absolute ones. As this difference has potentially important implications for the geodynamical interpretation of the model, we have examined its resolution with the synthetic tests presented in Figure 4. The two models present two alternatives for the low-velocity zone associated with the Patagonia slab window: a simple deep low-velocity anomaly or a low-velocity zone also extending eastwards beneath a faster continental region at the surface. As noted earlier, the inversion with relative kernels is clearly able to resolve the difference between the two models even though the area with high velocity at the surface is in a region with low resolution. The difference is far less clear in the models derived with the absolute kernels due to the blurring by extensive horizontally-lying anomalies. Between 200 and 300km depth, the low-velocity anomaly is replaced by a high-velocity region, exactly as we observe in the model resulting from the inversion of the data with absolute kernels (Figure 7, plot a).

6. Choice of phases and interference with other phases

In addition to the discussion above concerning how to use data with irregular coverage, we would like to briefly discuss an additional element regarding quality control of finite-frequency residuals that we have not seen discussed in other studies. As opposed to ray-based tomography where data are usually individual phases arrival times picked at onset time, finite-frequency tomography relies on correlation of filtered traces which intrinsically have a finite time length. Measuring the residuals by cross-correlation of the waveforms with the stack assumes that all waveforms are similar. Any distance-dependent variation in the waveform would produce a bias. The method is therefore more prompt to bias by interference between phases than onset-time based tomography and possible biases should be checked carefully. Our procedure has an intrinsic iterative acceptance criterion based on the similarity of each waveform with the stack. This is efficient in removing noisy individual waveforms but does not

protect from biases due to gradually changing waveforms due for example to interference with other phases than the phase of interest.

In the present study, we have used direct P and SH phases. As the region covered by the stations is 14 degrees in its largest dimension, a small set of stations may fall out of this range for some events and are then discarded. The lower epicentral limit is chosen to avoid the range where direct waves have triplications and therefore complex waveforms. The higher limit ensures that we do not include core-diffracted waves. We have tested if inclusion of core-diffracted phases P_{diff} could provide additional data. Although our data are filtered in a rather narrow frequency range, we observe that the shift in frequency content associated with getting further into the shadow zone introduces a bias in the residuals beyond the acceptable noise level. The time windows used to extract the data are of 20 and 70 seconds for the P waves at high and low frequencies respectively and 70 seconds for S waves. These windows need to be long enough for the filters to work satisfactorily. They may include other phases than the direct ones, in particular surface-reflected phases and core-reflected phases at the largest distances. Concerning surface-reflected phases, they interfere with the direct ones only for rather shallow events and have in these cases very similar slowness values. We have therefore considered that the waveform does not change significantly across the network, and that the slowness correction done when pre-aligning the data are valid for direct as well as reflected phases. This has been verified manually and many of our data are a combination of direct and surface-reflected waves, with the reflected ones dominating in cases of favorable focal mechanisms.

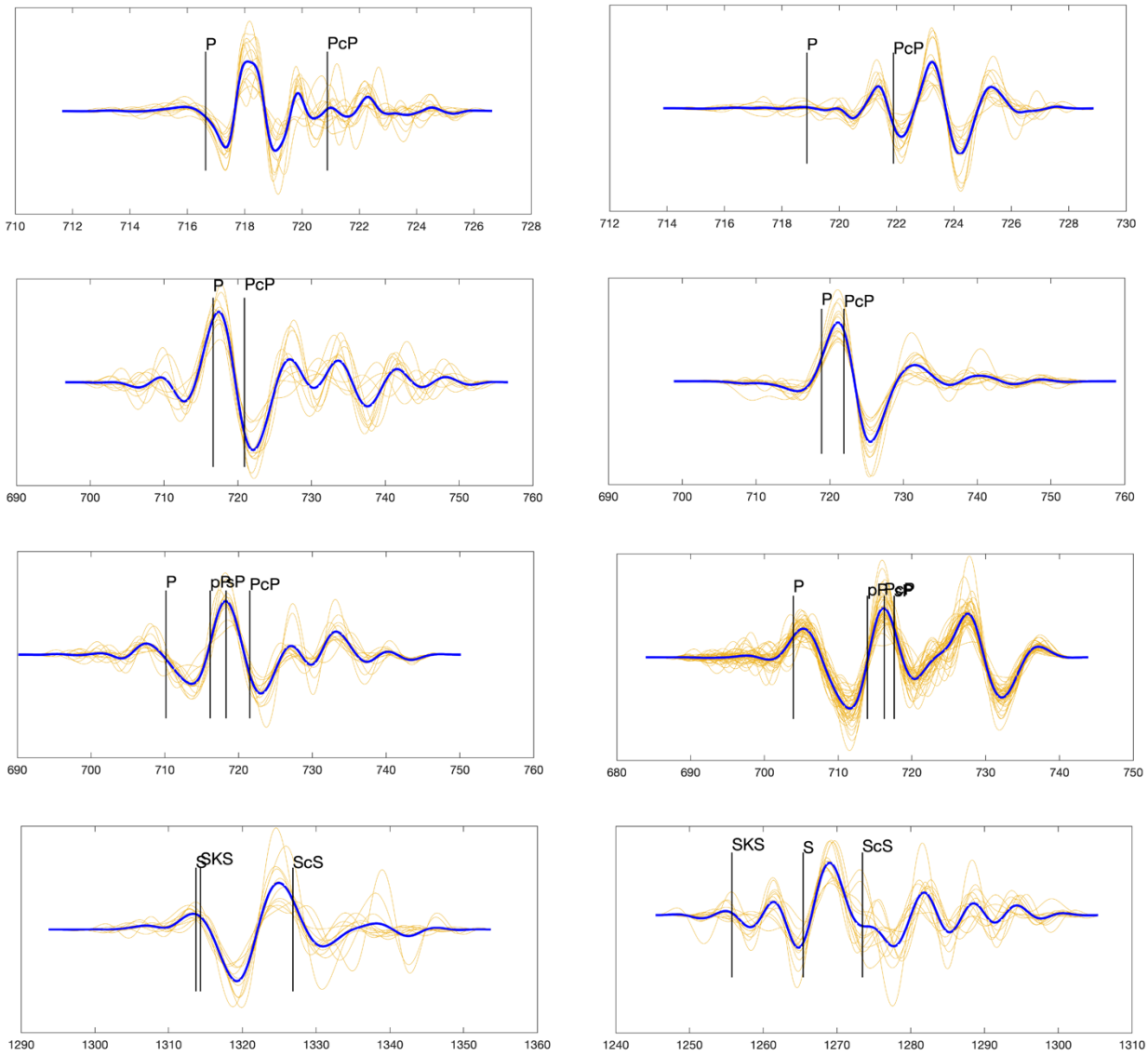

Figure 8. *Stack (blue lines) of data after alignment by ICCS (orange lines) for events in Fiji and Kermadec as a function of time (in seconds) annotated with the arrival times predicted by IASP91 at the center of the station network. The 2 upper plots are for P waves in the high-frequency range, those in the middle for P waves in the low-frequency range, and the bottom plots are for S waves. All cases shown on the left-hand side have been retained for inversion, while those on the right-hand side have been rejected.*

The situation is rather different for the core-reflected phases which arrive shortly after the direct phases which dive deep into the lower mantle. Despite similar paths, the difference in slowness between the direct waves and the core-reflected ones is large enough to introduce errors in the residuals if the core-reflected wave dominates the waveform. The amplitudes of the two waves are however not totally independent. Since the waves depart from the source

with very similar angles of incidence, they have similar amplitudes at the source and their amplitude ratio is dominantly related to the reflection coefficient at the CMB. This coefficient is smaller than 0.2 for P waves in the epicentral distance range 80° to 90° [Rost and Thomas, 2010]. This implies that the effect of the interference with the core-reflected phase should not be a major issue in most cases for P waves. This is different for SH waves as they fully reflect at the CMB. In addition, they may interfere with SKS waves. Also dominantly polarized as SV, SKS waves acquire a transverse component in cases of anisotropy, as for example observed in our study region [Ben-Mansour et al. 2022].

We have therefore introduced a rejection criterion in our data selection procedure. Events with a maximum amplitude of the stack arriving after the theoretical arrival of the core-reflected are automatically rejected. All other events which have core-reflected phases arriving within the selected time window are visually inspected before acceptance. Figure 8 shows examples of selected and rejected data. For our data set, rejection of possibly core-phase biased events is not a major problem for P waves since they mostly belong to the Kermadec-Tonga-Fiji area where the seismicity is plentiful For S waves, the selection is more difficult to do and interference with core phases may add noise in the data. In any case, we recommend attention to this potential issue and careful inspection of the waveforms.

7. Crustal correction

The near-vertical incidence of the direct P and SH waves used in general in regional body-wave tomography does not allow for resolving the crust, but variations in Moho depth and topography across the network affect the residuals and need to be accounted for. In regions where the crustal structure is too poorly known, one can assume that the crust affects the residuals in the same way for all events and contributes as a station term which can be inverted for during the tomography (e.g. Civiero et al., 2016). However, the most common practice is, **in** addition to a minor station term as in the present study, to correct for the crust using a global model such as CRUST1.0 [Laske et al., 2013] or a regional model. In Patagonia, we were able to use the regional crustal model from Mark et al. (2022), as presented in Ben-Mansour et al. (2025).

It is well-established that the reverberations in the crust affect the travel times at different frequencies in different ways, and that crustal delay times of high-frequency and low-frequency data may be significantly different, in particular in oceanic domains and regions of thick sedimentary basins [Obayashi et al. 2004; Yang and Shen, 2006; Ritsema et al., 2009;

Kolstrup and Maupin, 2015]. The crustal correction of finite-frequency travel time residuals should therefore be made frequency dependent. This is done in our study following the procedure of Kolstrup and Maupin (2015) which uses the reflectivity method [Levin and Park, 1997] applied in a 1-D seismic model below each station. An important point is that it is advantageous to perform the correction by appropriately shifting the time series with respect to each other before performing the stacking and cross-correlation procedure. There are two main reasons for that. Firstly, by correcting for known delays, we minimize the time differences between the time series, reducing the risk of cycle skipping, and ensuring a faster convergence of the stack. A second point, which is less obvious but nonetheless important, is that relative body wave tomography assumes that the mean of the residuals for every event is zero. Conducting crustal correction after measuring the residuals is likely to change the mean of the data set, requiring further adjustment of the residuals, a pretty unnecessary complicating step.

8. Discussion and conclusion

The advantage of combining data from different networks will vary from case to case. Often it will be a matter of extending the region of study. In the present case, it is a matter of getting the big picture in addition to a better resolution in a region of particular interest from a geodynamical point of view. We see for example that with our data coverage using the relative kernels is crucial for imaging the eastward extension at depth of the Patagonia slab window, which is of major geodynamical interest.

In our application, replacing the relative kernels by absolute kernels supplemented by event terms produce a clearly degraded velocity model. Actually, the introduction of event terms did not affect the model compared with an inversion with absolute kernels only. We could not find damping values of the different terms that would solve the problem in the framework of our data-adaptive multiscale inversion regularization. Event terms have been used for taking into account station heterogeneity [Bezeda et al., 2010; Youssof et al., 2015], but we are not aware of synthetic tests to study their efficiency with other regularization approaches than ours. It could be interesting to test this further before future applications.

Instead of using relative kernels, one can invert the differences in residuals between pairs of stations. This also allows combining data that have not been registered at all stations simultaneously. This procedure was chosen by Kondo et al. (2024) for a P-wave data set partly

overlapping with the one we use here. The kernels to be used in that case are then just the difference between the two absolute kernels of the pair of stations involved [Hung et al., 2000]. The main disadvantage of this method is to increase the size of the inverse problem since the number of data points per event is basically the square of the number of original residuals, without actually increasing the information content. Depending on how the residuals are calculated, one also loses the great advantage of MCCC where the compatibility of the residual differences between pairs of stations is used for data quality analysis and error bar assignment. Other alternatives are to use a 3D reference model derived from surface wave inversion [Rawlinson and Fishwick, 2012], to anchor residuals to some permanent stations or to link the residuals to a global model, moving from relative residuals to absolute ones [Chevrot 2002; Weidle and Widiyantoro 2005; Burdick et al. 2008; Boyce et al. 2017]. The advantages and disadvantages of these alternatives are discussed more in details in Maupin (2021).

We have also presented which selection criteria we have used to avoid bias in data by interference with core phases at large epicentral distances. Due to the length of the time windows on which we have to operate, using low-frequency data is more challenging than using high-frequency data or picking arrival times. This is particularly true for S wave data at epicentral distances close to the shadow zone. The quality of the inverted model is totally dependent on a correct selection of the data on which to measure residuals. Although we experience that the ICCS algorithm is very efficient in removing noisy traces and cases with incoherent waveforms, an automatic procedure is not able to deal with all cases and manual review of all data is an advantage.

Although regional body-wave tomography only provides relative velocity anomalies, it is a popular method for exploiting data from numerous seismological station deployments. Especially in association with surface wave studies, it can provide the resolution necessary to answer intricate geodynamical questions difficult to address with global models. In this paper, we have shared some recommendations for data processing and inversion gained through our experiences with a tomography of Patagonia and shown in particular that data from asynchronous networks can be combined and that usage of relative sensitivity kernels is superior to the introduction of event terms to take into account station distribution heterogeneity.

Acknowledgements

We thank two anonymous reviewers and the editor Ian Bastow for their constructive comments, in particular concerning event terms. The authors would like to thank Christine Thomas, University of Munster, for advice concerning interference of direct waves with core phases. The computations have been made using a modified version of the software for finite-frequency body wave tomography kindly provided by Shu-Huei Huang, National Taiwan University. Waveforms and metadata were accessed via the EarthScope Data Management System. This research was funded by the National Science Foundation under grant EAR-1714154: Collaborative Research: Solid Earth Response of the Patagonian Andes to Post-Little Ice Age Glacial Retreat. VM is supported by the Research Council of Norway's project 332523 (Center for Planetary Habitability). Figures were produced using GMT software [Wessel et al., 2013] using perceptually uniform colour maps generated by Fabio Crameri [Crameri, 2018] and available at http://www.fabiocrameri.ch/colourmaps.php.

564 References

565 Aki, K, Christoffersson, A, Husebye, E (1977), Determination of the three-dimensional seismic
566 structure of the lithosphere, Journal of Geophysical Research, 82 ,2, 277--296.
567
568 Ben-Mansour, W, Wiens, DA, Mark, HF, Russo, RM, Richter, A, Marderwald, E, Barrientos, S
569 (2022), Mantle flow pattern associated with the Patagonian slab window determined from
570 azimuthal anisotropy, Geophysical Research Letters, 49,18, e2022GL099871.
571
572 Ben-Mansour, W., Maupin, V, Wiens, DA, Richter, A (2025), Deep source regions for
573 Patagonia backarc volcanism imaged by finite frequency body wave tomography, Geophysical
574 Research Letters, 52, e2025GL115915.
575
576 Bezada, MJ, Levander, A, Schmandt, B (2010), Subduction in the southern Caribbean:
577 Images from finite-frequency P wave tomography, Journal of Geophysical Research: Solid
578 Earth, 115, B12.
579
580 Boyce, A, Bastow, ID, Rondenay, S, Van der Hilst, RD (2017), From Relative to Absolute
581 Teleseismic Travel Times: The Absolute Arrival-Time Recovery Method (AARM), Bulletin of
582 the Seismological Society of America, 107, 5, 2511—2520.
583
584 Burdick, S, Li, C, Martynov, VIV, Cox, Tr, Eakins, J, Mulder, T, Astiz, L, Vernon, FL, Pavlis,
585 GL, van der Hilst, RD (2008), Upper mantle heterogeneity beneath North America from travel
586 time tomography with global and USArray transportable array data, Seismological Research
587 Letters,79, 3, 384—392.
588
589 Chevrot, S (2002), Optimal measurement of relative and absolute delay times by simulated
590 annealing, Geophysical Journal International, 151, 1, 164—171.
591
592 Chevrot S, Sylvander, M, RESIF (2017), Seismic network X7: PYROPE PYRenean
593 Observational Portable Experiment, https://doig.org/10.15778/ RESIF.X72010.
594
595 Civiero, C, Goes, S, Hammond, JOS, Fishwick, S, Ahmed, A, Ayele, A, Doubre, C, Goitom,
596 B, Keir, D, Kendall, JM, Leroy, S, Ogubazghi, O, Rumpker, G, Stuart, GW (2016), Small-scale

thermal upwellings under the northern East African Rift from S travel time tomography, Journal Geophysical Research, Solid Earth, 121, 7395–7408, doi:10.1002/2016JB013070.

Crameri, F (2018). Scientific colour maps: perceptually uniform and colour-blind friendly, doi: 10.5281/zenodo.1243862, code repository at www.fabiocrameri.ch/colourmaps

Dahlen, FA , Hung, S-H, Nolet, G (2000), Frechet kernels for finite-frequency traveltimes—I. Theory, Geophysical Journal International,141,1,157—174.

Diaz, J, Villasenor, A, Gallart, J, Morales, J, Pazos, A, Cordoba, D, Pulgar, J, Garcia-Lobon, JL, Harnafi, M and others (2009), The IBERARRAY broadband seismic network: a new tool to investigate the deep structure beneath Iberia ,Orfeus Newsletter,8,2, 1—6.

Dong, S-W , Li, T-D , Lu, Q-T, Gao, R, Yang, J-S, Chen, X-H, Wei, W-B, Zhou, Q,SinoProbe team and SinoProbe team (2013), Progress in deep lithospheric exploration of the continental China: A review of the SinoProbe,Tectonophysics,606,1—13.

Engdahl E.R, Di Giacomo D., Sakarya B., Gkarlaouni C. G., Harris J., Storchak D. A.,2020. ISC- EHB 1964–2016, an Improved Data Set for Studies of Earth Structure and Global Seismicity, Earth and Space Science, Vol 7, e2019EA000897.

Fichtner, A, Trampert, J, Cupillard, P, Saygin, E, Taymaz, T, Capdeville, Y, Villasenor, A (2013), Multiscale full waveform inversion, Geophysical Journal International, 194, 1,534—556.

Hetenyi, G, Molinari, I, Clinton, J, Bokelmann, G, Bondar, I, Crawford, WC, Dessa, JX, Doubre, C, Friederich, W, and Fuchs, F, and others (2018), The AlpArray seismic network: a large-scale European experiment to image the Alpine Orogen, Surveys in geophysics,39,1009—1033.

Hung, S-H and Dahlen, FA and Nolet, G. (2000), Frechet kernels for finite-frequency traveltimes: II. Examples, Geophysical Journal International, 141, 1,175--203.

Hung, SH, Chen, WP, Chiao, LY (2011), A data-adaptive, multiscale approach of finite-frequency, traveltime tomography with special reference to P and S wave data from central Tibet, Journal of Geophysical Research: Solid Earth, 116, B6.

IRIS Transportable Array. (2003). USArray Transportable Array [Data set]. International Federation of Digital Seismograph Networks. https://doi.org/10.7914/SN/TA

Kolstrup M.L. and Maupin, V. (2015), Measuring and crust-correcting finite-frequency travel time residuals – application to southwestern Scandinavia, Solid Earth, 6, 1117-1130.

Kondo, Y, Obayashi, M, Sugioka, H, Shiobara, H, Ito, A, Shinohara, M, Iwamori, H, Kinoshita, M, Miller, M, Tassara, C, Ojeda, J (2024), Seismic image of the central to southern Andean subduction zone through finite-frequency tomography, Journal of Geophysical Research: Solid Earth, 129,11.

Laske, G, Masters, G, Ma, Z, Pasyanos, M (2013), Update on CRUST1. 0- A 1-degree global model of Earth's crust,,Geophysical research abstracts,15,15,2658.

Levin, V and Park, J (1997), P-SH conversions in a flat-layered medium with anisotropy of arbitrary orientation, Geophysical Journal International, 131,2, 253--266.

Lou, X, Van Der Lee, S, Lloyd, S (2010), AIMBAT: A python/matplotlib tool for measuring teleseismic arrival times, Seismological Research Letters, 84, 1, 85--93.

Maupin, V, Kolstrup, ML (2015), Insights in P-and S-wave relative traveltime tomography from analysing finite-frequency Frechet kernels, Geophysical Journal 202, 3,1581--1598.

Maupin, V (2021), Combining asynchronous data sets in regional body-wave tomography, Geophysical Journal International, 224,1, 401--415.

660 Mark, HF, Wiens, Douglas A, Ivins, Erik R, Richter, A, Ben-Mansour, W, Magnani, MB,
661 Marderwald, E, Adaros, R, Barrientos, S (2022), Lithospheric erosion in the Patagonian slab
662 window, and implications for glacial isostasy, Geophysical Research Letters, 49, 2,
663 e2021GL096863.
664
665 Miller, M, Priestley, K, Tilmann, F, Bataille, K, Iwamori, H (2023), P wave teleseismic tomography
666 of the subducted Chile rise, Journal of South American Earth Sciences, 128, 104474.
667
668 Obayashi, M., Suetsugu, D., and Fukao, Y.: PP-P differential traveltime measurement with crustal
669 correction (2004), , Geophysical Journal International, 157, 1152–1162.
670
671 Rawlinson, N, Fishwick, S (2012). Seismic structure of the southeast Australian lithosphere from
672 surface and body wave tomography, Tectonophysics, 572, 111-122.
673
674 Ritsema, J, Van Heijst, HJ , Woodhouse, JH, Deuss, A (2009), Long-period body wave travel
675 times through the crust: implication for crustal corrections and seismic tomography, Geophysical
676 Journal International, 179, 2,1255--1261.
677
678 Rost S and Thomas C (2010). High resolution CMB imaging from migration of short-period core
679 reflected phases, Phys. Earth planet. Int., 183, 143-150, doi:10.1016/j.pepi.2010.04.005.

680 Russo, RM (2010), Subduction of the Chile Ridge: Upper mantle structure and flow, Gsa
681 Today,20.
682
683 Schmandt, B and Humphreys, E (2010), Seismic heterogeneity and small-scale convection in the
684 southern California upper mantle, Geochemistry, Geophysics, Geosystems,11,5.
685
686 Thybo, H, Bulut, N, Grund, M, Mauerberger, A, Makushkina, A, Artemieva, IM, Balling, N,
687 Gudmundsson, O, Maupin, V, Ottemoller, L, Ritter, J, Tilmann, F (2021), ScanArray—A
688 Broadband Seismological Experiment in the Baltic Shield, Seismological Research Letters 92 (5):
689 2811–2823.
690

691 Tromp, J, Tape, C, Liu, Q (2005) Seismic tomography, adjoint methods, time reversal and
692 banana-doughnut kernels, Geophysical Journal International, 160, 1, 195, 216.
693
694 Tromp, J (2020), Seismic wavefield imaging of Earth's interior across scales, Nature Reviews
695 Earth & Environment, 1, 1, 40-53.
696
697 VanDecar, JC and Crosson, RS (1990), Determination of teleseismic relative phase arrival times
698 using multi-channel cross-correlation and least squares, Bulletin of the Seismological Society of
699 America, 80,1, 150--169.
700
701 Wessel, P., Smith, W., Scharroo, R., Luis, J. , Wobbe, F., (2013). Generic Mapping Tools:
702 improved version released, EOS, Trans. Am. geophys. Un., 94, 409–410.
703
704 Weidle, C, Widiyantoro, S, (2005) Improving depth resolution of teleseismic tomography by
705 simultaneous inversion of teleseismic and global P-wave traveltime data—application to the
706 Vrancea region in Southeastern Europe, Geophysical Journal International,162,3,811—823.
707
708 Veisi, M, Sobouti, F, Chevrot, S, Abbasi, M, Shabanian, E (2021), Upper mantle structure under
709 the Zagros collision zone; insights from 3D teleseismic P-wave tomography, Tectonophysics, 819,
710 229106.
711
712 Yang, T and Shen, Y (2006), Frequency-dependent crustal correction for finite-frequency seismic
713 tomography, Bulletin of the Seismological Society of America, 96, 6 ,2441--2448.
714
715 Youssof, M, Thybo, H, Artemieva, IM, Levander, A (2015), Upper mantle structure beneath
716 southern African cratons from seismic finite-frequency P-and S-body wave tomography, Earth
717 and Planetary Science Letters, 420, 174—186.
718

719 Appendix A: Results for event and stations terms in different cases

720

721

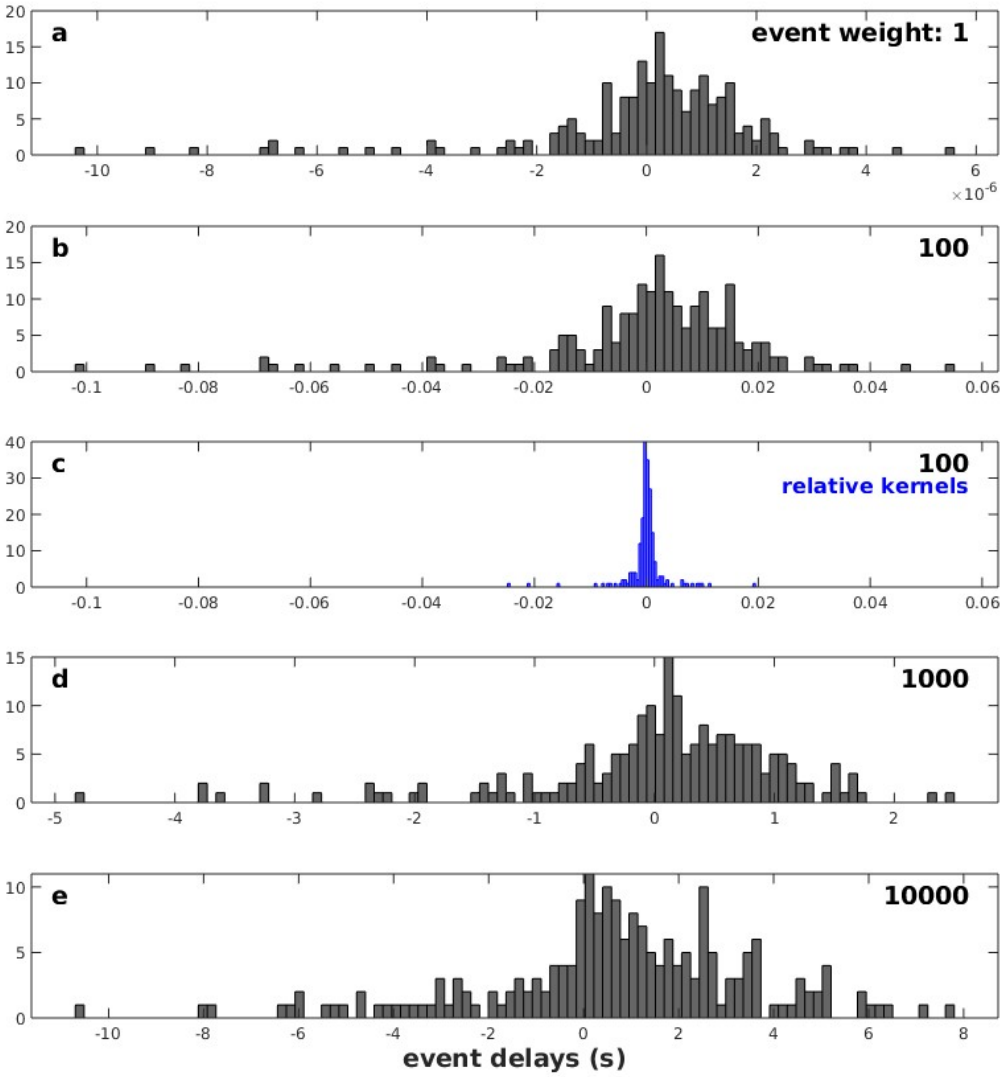

722 **Figure A1**. *the same as Figure 5 for the synthetic model L1.*

723

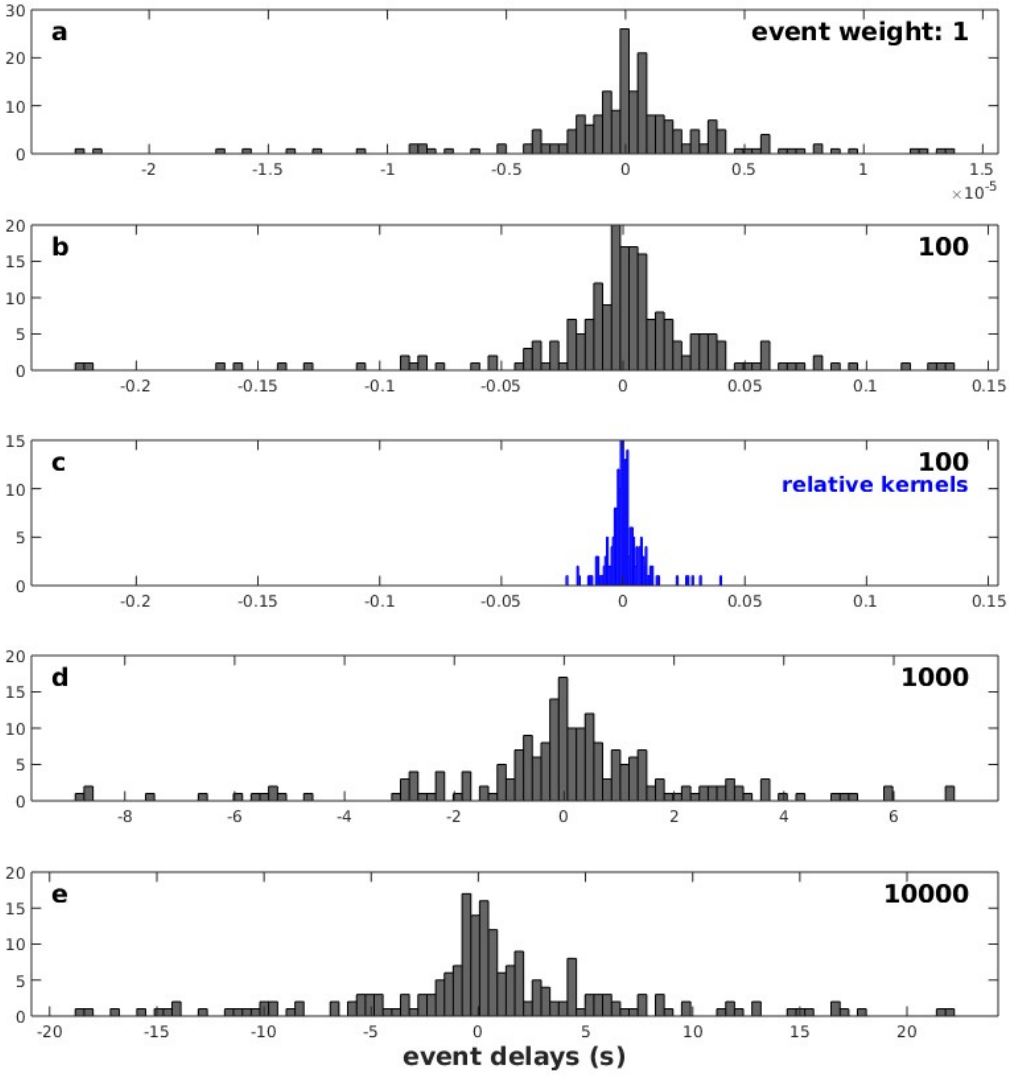

724

725 **Figure A2.** ***The same as Figure 5 for the real data.***

726

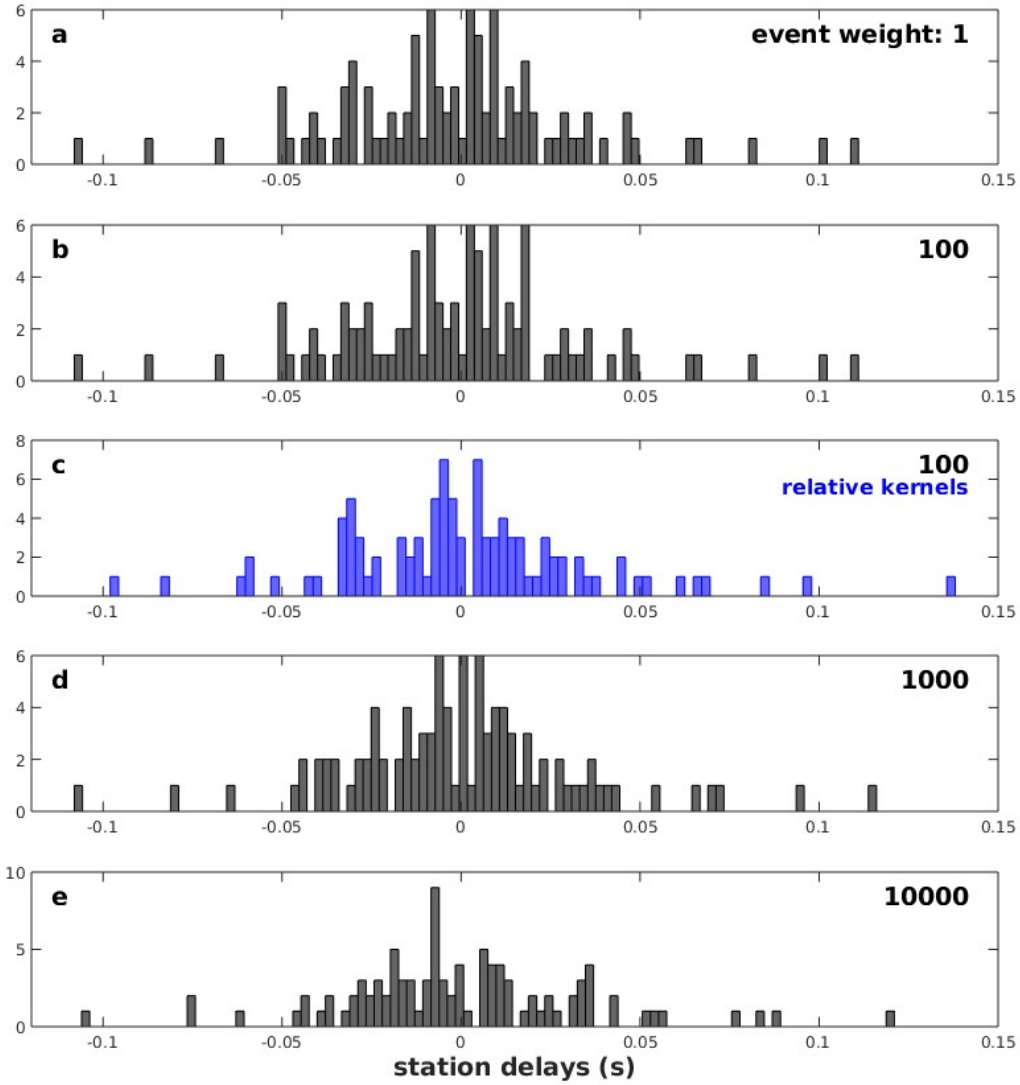

Figure A3. *Histograms of the station terms obtained with the real data and different weights for the event terms. The weight for the station term is unchanged and put to 100 in all cases. This shows that changing the weight of the event term has very little impact on the values of the station terms, and that one can therefore consider that the trade-off between the two types of terms is not significant. Using relative or absolute kernels has also very little impact on these values.*

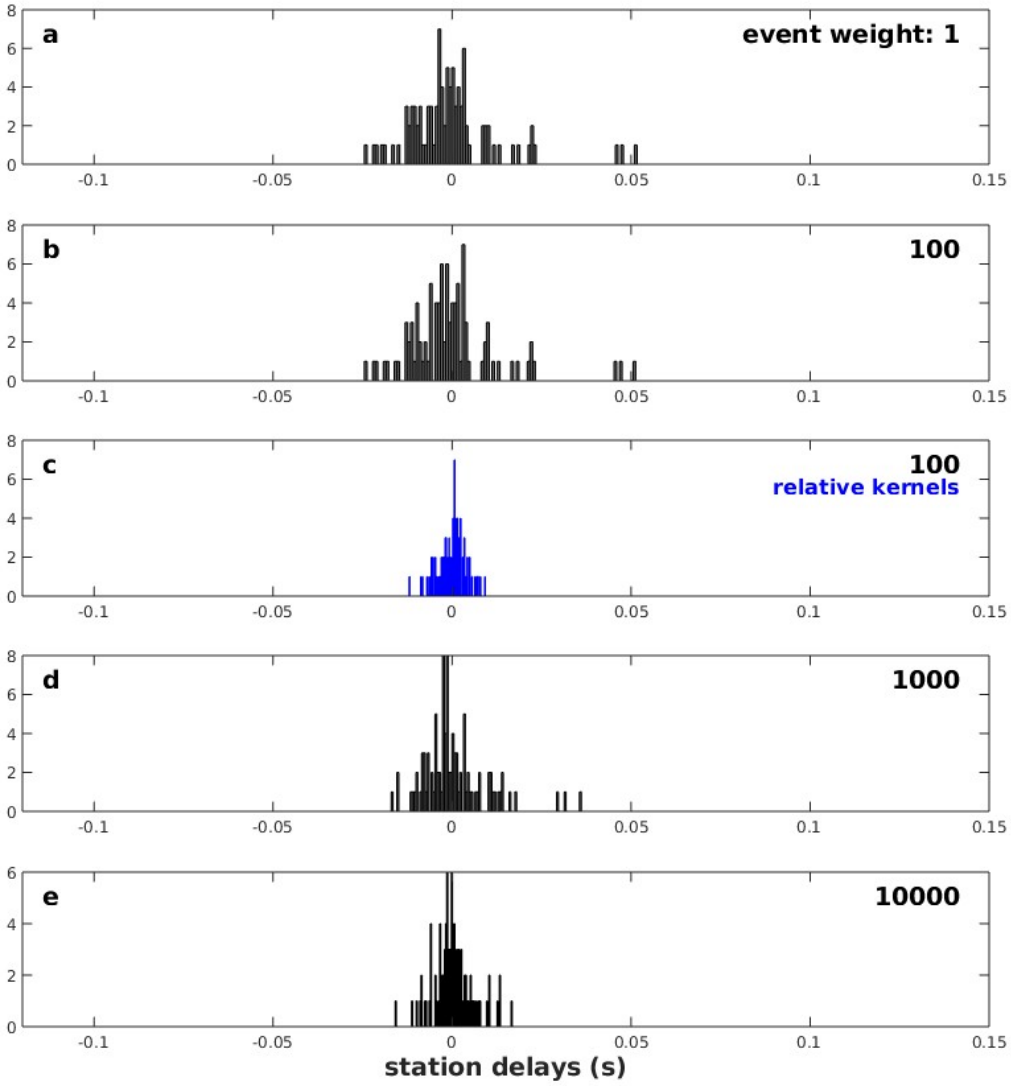

Figure A4. *The same as Figure A3 for the synthetic model L2. As anticipated, the stations terms are very small in this synthetic case with no crustal variation.*